Synchondrosis fusion contributes to the progression of postnatal craniofacial dysmorphology in syndromic craniosynostosis.

Yukiko Hoshino[1,2†], Masaki Takechi[1,3†]*, Mehran Moazen[4], Miranda Steacy[5], Daisuke Koyabu[1,6], Toshiko Furutera[1,3], Youichirou Ninomiya[7], Takashi Nuri[8], Erwin Pauws[5], Sachiko Iseki[1]*

1. Department of Molecular Craniofacial Embryology, Graduate School of Medical and Dental Sciences, Tokyo Medical and Dental University (TMDU), Japan.
2. Office of New Drug V, Pharmaceuticals and Medical Devices Agency (PMDA), Japan.
3. Department of Anatomy and Life Structure, Juntendo University Graduate School of Medicine, Japan
4. Department of UCL Mechanical Engineering, University College London, UK.
5. Institute of Child Health, Great Ormond Street, University College London, UK.
6. Research and Development Center for Precision Medicine, Tsukuba University, Japan.
7. Research Organization of Information and Systems, National Institute of Informatics, Japan
8. Department of Plastic and Reconstructive Surgery, Osaka Medical and Pharmaceutical University, Japan

[†]These authors contributed equally to this work.

*Correspondence to:
Masaki Takechi
Section of Molecular Craniofacial Embryology,
Graduate School of Medical and Dental Sciences, Tokyo Medical and Dental University (TMDU), 1-5-45 Yushima, Bunkyo-ku, Tokyo 113-8549 JAPAN.
E-mail: takechi.emb@tmd.ac.jp
Phone: +81-3-5803-5579
Fax: +81-3-5803-0213
ORCID ID: 0000-0001-7279-9243

Sachiko Iseki
Section of Molecular Craniofacial Embryology,
Graduate School of Medical and Dental Sciences, Tokyo Medical and Dental University (TMDU), 1-5-45 Yushima, Bunkyo-ku, Tokyo 113-8549 JAPAN.
E-mail: s.iseki.emb@tmd.ac.jp
Phone: +81-3-5803-5579
Fax: +81-3-5803-0213
ORCID ID: 0000-0001-8448-9410

Abstract

Syndromic craniosynostosis (CS) patients exhibit early, bony fusion of calvarial sutures and cranial synchondroses, resulting in craniofacial dysmorphology. In this study, we chronologically evaluated skull morphology change after abnormal fusion of the sutures and synchondroses in mouse models of syndromic CS for further understanding of the disease. We found fusion of the inter-sphenoid synchondrosis (ISS) in Apert syndrome model mice (*Fgfr2*$^{S252W/+}$) around three weeks old as seen in Crouzon syndrome model mice (*Fgfr2c*$^{C342Y/+}$). We then examined ontogenic trajectories of CS mouse models after three weeks of age using geometric morphometrics analyses. Antero-ventral growth of the face was affected in *Fgfr2*$^{S252W/+}$ and *Fgfr2c*$^{C342Y/+}$ mice while Saethre–Chotzen syndrome model mice (*Twist1*$^{+/-}$) did not show the ISS fusion and exhibited a similar growth pattern to that of control littermates. Further analysis revealed that the coronal suture synostosis in the CS mouse models induces only the brachycephalic phenotype as a shared morphological feature. Although previous studies suggest that the fusion of the facial sutures during neonatal period is associated with midface hypoplasia, the present study suggests that the progressive postnatal fusion of the cranial synchondrosis also contributes to craniofacial dysmorphology in mouse models of syndromic CS. These morphological trajectories increase our understanding of the progression of syndromic CS skull growth.

Keywords

craniosynostosis, Apert syndrome, Crouzon syndrome, Saethre–Chotzen syndrome, geometric morphometrics, inter-sphenoid synchondrosis, coronal suture, midfacial hypoplasia.

1. Introduction

The skull vault is composed of several bony elements that are connected by the cranial sutures. The suture is a fibrous tissue formed by undifferentiated mesenchymal cells and osteoblast precursors (Opperman, 2000; Beederman et al., 2014). The cranial sutures of mammals allow temporary deformation during parturition and play a crucial role as growth sites of the developing skull (Flaherty et al., 2016). In humans, the majority of the cranial sutures are replaced with bony tissues in adulthood except for the metopic suture between the frontal bones that fuses around two years old (Cohen, 2005). Synchondroses in the cranial base are also growth centers of craniofacial skeleton after birth (Krishan and Kanchan, 2013). The inter-sphenoid synchondrosis (ISS) and the sphenoid-occipital synchondrosis (SOS) are the main synchondroses present along the midline of the skull. In humans, the ISS begins to fuse before birth and completely ossifies by two or three years old (Hayashi, 2003; Madeline and Elster,1995) whereas the SOS remains patent up to the adolescent, which indicates that the SOS contributes to postnatal craniofacial skeletal growth (Cendekiawan et al., 2010).

Craniosynostosis (CS) defined as premature fusion of one or more cranial suture(s) occurs approximately 1 in 2,000-2,500 newborns (Boulet et al., 2008). CS leads to morphological abnormalities, such as deformation of the cranial vault and facial asymmetry, accompanied by increased intracranial pressure and dysfunction of the brain (Slater et al., 2008). CS is classified into the non-syndromic and the syndromic, the latter usually demonstrates the severe phenotypes (Flaherty et al., 2016). Mutations in fibroblast growth factor type 2 receptor (*FGFR2*) are associated with Apert syndrome characterized by CS with cranial, neural, limb, and visceral malformations (OMIM#101200). The majority of Apert syndrome patients carry one of two mutations associated with the change of Serine (Ser252Trp) and Proline (Pro253Arg) in exon IIIa that comprises the linker region between the second and the third extracellular immunoglobulin-like domains of the ligand binding site (Wilkie et al., 1995). These mutations are gain-of-function types and alter the ligand-binding affinity and specificity (Plotnikov et al., 2000; Ibrahimi et al., 2001), resulting in abnormal cell proliferation, differentiation, and migration (Ornitz and Marie, 2002). Anomalies and dysfunctions in Apert syndrome include midface hypoplasia, hypertelorism, syndactyly of hand and feet, and hearing loss (Lance and Governale, 2015). Crouzon syndrome is also caused by mutations in *FGFR2*, a missense mutation at Cysteine 342 in exon 9 (Cys342Tyr) is the most common in the disease, resulting in ligand-independent receptor dimerization (Fenwick et.al., 2014). Patients with Crouzon syndrome often exhibit hypertelorism and exophthalmos (OMIM#123500) (Lance and Governale, 2015). Haploinsufficiency of *TWIST1* gene induces a syndromic CS, Saethre–Chotzen syndrome (OMIM #101400), with brachydactyly, facial dysmorphism and limb abnormalities (El Ghouzzi et al., 1997; Paznekas et al., 1998). In these syndromes, the fusion of the coronal suture is the main phenotype, and the fusion is initiated prenatally and commonly followed by the fusion of other cranial sutures postnatally (Lance and Governale, 2015). Regarding the cranial base in syndromic CS patients, both Apert and Crouzon syndrome patients exhibit earlier closure of the SOS

compared to the matched controls, the closure begins around two to three years old (Mcgrath et al., 2012; Tahiri et al., 2014). Of note, the fusion has not been reported in Saethre–Chotzen syndrome patients.

CS mice are invaluable models to advance our understanding of syndromic CS in humans (Lee et al., 2019). One of the mouse models of Apert syndrome, *Fgfr2*$^{S252W/+}$ mouse, demonstrates premature craniosynostosis and skull malformation as well as abnormalities of internal organs (Figure 1b, Chen et al. 2003; Wang et al., 2005). About 80% of *Fgfr2* $^{S252W/+}$ mice show partial to complete fusion of the coronal suture at postnatal day (P) 0 (Motch Perrine et al., 2014). The *Fgfr2c*$^{C342Y/+}$ mouse has been reported as a mouse model of Crouzon syndrome (Figure 1c), showing shortened face, protruding eyes, and premature fusion of the cranial sutures (Eswarakumar et al., 2004). Martinez-Abadias et al. (2013) noted that over 95% of *Fgfr2c*$^{C342Y/+}$ mutant mice at P0 exhibit partial to complete bilateral coronal suture fusion. Postnatal fusion of the ISS is also reported in the mutant with various genetic backgrounds (Liu et al., 2013). *Twist1* heterozygous mice (*Twist1*$^{+/-}$) recapitulate the phenotype clinically observed in Saethre–Chotzen syndrome patients (El Ghouzzi et al., 1997). *Twist1*$^{+/-}$ mice postnatally demonstrate the fusion of the coronal suture either in bilateral or unilateral (Figure 1d) in about 80% of the skulls by P15. On the other hand, the ISS remains patent up to the adult stage (Carver et al., 2002; Parsons et al., 2014; Nuri et al, 2022) as seen in wild-type mice.

Contrary to description of skull morphology by qualitative observation, quantitative analysis such as geometric morphometrics (Adams et al., 2004) provides a more accurate description and evaluation of craniofacial dysmorphogenesis, and these data may contribute to improved clinical diagnosis and subsequent therapeutic strategies. Cranial morphologies of *Fgfr2*$^{S252W/+}$ and *Fgfr2*$^{P253R/+}$ mice, Apert syndrome models, can be distinguished as early as P0 by principal component analysis (PCA) (Martinez-Abadias et al., 2010). Growth Difference Matrix Analysis (GDMA) has revealed that mutant and non-mutant mice display statistically different growth trajectories, and the difference becomes larger with age (Motch Perrine et al., 2014). A Crouzon mouse model with *Fgfr2c*$^{C342Y/+}$ mutation at P0 shows significant features, expansion of height and width of the posterior region of the cranial vault, and the length of the anterior part of the facial skeleton including nasal bones shows shorter than wild-type mice (Martinez-Abadias et al., 2013). Parsons et al. (2014) reported that the skull morphology of *Twist1*$^{+/-}$ mice at P15 is induced not simply by compensatory growth disturbances resulting from the coronal suture fusion. Although the fusion of the coronal suture is the main phenotype of the patients and the model mice, these observations suggest that morphological abnormalities are induced not only by the coronal suture fusion but also by other factors. Given that dysmorphology of the skull and the brain increases with age in CS patients (Breakey et al., 2018), ontogenic trajectories of the skull shape may be fundamental information for understanding the nature of the syndromic CS cases caused by a specific gene mutation.

Previous reports on CS mouse models using geometric morphometric approaches mainly revealed morphological features of prenatal or neonatal skull shape, the relation to brain development, and the interaction between craniofacial dysmorphogenesis and coronal suture patency. However, evaluation of skull

morphology after abnormal fusion of cranial sutures and synchondroses in CS mouse models has not been reported. As described in the existing literature, the three CS mouse models (*Fgfr2*$^{S252W/+}$, *Fgfr2c*$^{C342Y/+}$ and *Twist1*$^{+/-}$) usually exhibit closure of the coronal suture by three weeks old (Motch Perrine et al., 2014; Martinez-Abadias et al., 2013; Nuri et al., 2022). In addition, *Fgfr2c*$^{C342Y/+}$ mice have the fusion of the ISS by four weeks old (Liu et al., 2013) whereas wild-type mice maintain patency of the ISS and the SOS up to the adult stage. In this study, we therefore investigated the growth pattern of each CS mouse model using geometric morphometric analysis focusing on the postweaning period, corresponding approximately to two to three years old onward in humans based on the skull growth (Libby et al., 2017; Wei et al., 2017).

2. Materials and Methods

2.1 Mice

Twist1$^{+/-}$ mice (Chen and Behringer, 1995) and *Fgfr2*$^{S252W/+}$ mice (Chen et al. 2003; Wang et al. 2005) were maintained on a C57Bl/6J background (Sankyo Labo Service Corporation, Inc. Tokyo Japan), and *Fgfr2c*$^{C342Y/+}$ mice (Eswarakumar et al., 2004) were maintained on a CD-1 genetic background. The sample sizes of *Twist1*$^{+/-}$, *Fgfr2*$^{S252W/+}$, *Fgfr2c*$^{C342Y/+}$ and their littermate controls, which include either EIIa-Cre or *Fgfr2*$^{ploxpneo\text{-}S252W}$ positive mice, for this study are shown in TableS1. In our *Fgfr2* $^{S252W/+}$ colony, only individuals without fusion of the coronal suture survived after three weeks old. Three types of mixed anesthetic agent (Kawai et al., 2011) were injected to each mouse before micro-computed tomography (μCT) scanning. Antagonistic agent (Kawai et al., 2011) was injected at three, five, and seven weeks old for awakening while euthanasia was carried out by cervical dislocation at nine weeks old for *Twist1*$^{+/-}$ and *Fgfr2* $^{S252W/+}$ mice. *Fgfr2c*$^{C342Y/+}$ mice were euthanized using carbon dioxide and were kept in formaldehyde until they were μCT scanned. Animal experiments were conducted in accordance with protocols approved by the Institutional Animal Care and Use Committee of Tokyo Medical and Dental University (A2017-202C2, A2018-048C, A2019-060C2) and approved by the UK Home Office and performed as part of a Project License (PP8161503) under the UK Animals (Scientific Procedures) Act 1986.

2.2 μCT scanning

μCT images of heads of *Twist1*$^{+/-}$ mice and *Fgfr2* $^{S252W/+}$mice were acquired using Inspexio SMX-100CT (Shimadzu, Japan) with the X-ray source at 50-100 tube kV, 30-50 μA tube current. The whole skull was first scanned with voxel size ranging 0.061-0.063 mm, and then the cranial base was additionally rescanned with 0.013-0.015 mm voxel sizes for further detailed observation. μCT images of heads of *Fgfr2c*$^{C342Y/+}$ mice were acquired by X-Tek HMX 160 (XTek Systems Ltd, Tring, Herts., UK). The images had a voxel size of 0.02 mm. Three dimensional (3D) reconstruction of the skull was conducted using Avizo 6.3 (Visualization Sciences Group, USA, RRID:SCR_014431). 3D surfaces were reconstructed with Isosurface function in Avizo 6.3.

2.3 Sample preparation for histological analysis

The cranial base of *Fgfr2*$^{S252W/+}$ and *Fgfr2c*$^{C342Y/+}$ mice were dissected and fixed in 4% PFA, Bouin's solution, Carnoy's solution, or 70% ethanol, then demineralized in either 10% EDTA 2Na solution or 10% citric acid in 22.5% formic acid. The samples were embedded in paraffin after dehydration, and sagittal sections were obtained at 7-8 μm thickness for Hematoxylin-Eosin staining. The stained slides were cleared by xylene and applied to mounting agent for observation.

2.4 Landmark Data Collection and Shape analysis

Landmark-based geometric morphometrics were conducted to assess the growth pattern of each mouse model. 33 landmarks (Figure S1) were placed by Landmarks function in Avizo 6.3. Morpho J v1.07 (RRID:SCR_016483) was used for statistical analyses of acquired landmarks. All geometric morphometric analyses were applied to each genotype of mice regardless of sex because our preliminary analysis showed no significant sexual difference in the skull shape (data not shown). Generalized Procrustes analysis with superimposition was applied to normalize the size and align size-free shape information of skull landmarks regardless of size (Klingenberg, 2011). Centroid size was computed for each sample as the square root of the total sums of distances between each landmark coordinate. In order to extract the group differences, canonical variates analysis (CVA), which maximizes the separation of defined groups such as genotypes and ages (Klingenberg et al., 2011), was applied to landmark configuration of *Fgfr2*$^{S252W/+}$, *Fgfr2c*$^{C342Y/+}$, and *Twist1*$^{+/-}$ mice, and littermate controls grouped by age and genotype. In order to assess the overall variation of samples and covariation of landmarks, PCA was applied to landmark configuration of all CS mouse models with coronal suture fusion. Allometric effect in skull shape was assessed by linear regressions between centroid sizes and CVA or PCA scores.

2.5 Statistics

Pearson's correlation and statistical analysis were performed by Excel (Microsoft, USA, RRID:SCR_06137) or PRISM ver. 6.01 (GraphPad Software, USA, RRID:SCR_005375). P values of <0.05 were considered significant in Student's t-test.

3. Results

3.1 *Fgfr2*$^{S252W/+}$ mice showed abnormalities of the synchondroses in the cranial base after weaning

It was previously reported that a Crouzon syndrome mouse model (*Fgfr2c*$^{C342Y/+}$) and an Apert syndrome mouse model (*Fgfr2*$^{P253R/+}$) exhibit fusion of the ISS by four weeks old and P9, respectively (Liu et al., 2013; Yin et al., 2008). In contrast, the synchondroses appear normal at P18 in another Apert mouse model (*Fgfr2*$^{S252W/+}$) (Chen et al. 2003), therefore, we carefully observed the cranial base of *Fgfr2*$^{S252W/+}$ mice at later stages. The μCT images revealed that the ISS was partially fused in two out of five (2/5) and 5/5 *Fgfr2*$^{S252W/+}$ mice, at three and five weeks old, respectively (Figure 1g, h), while the littermate controls did not show the fusion (Figure 1e, f, white arrow). All *Fgfr2*$^{S252W/+}$ mice at nine weeks old showed fusion of the ISS (4/4) while 3/4 littermate controls did not show the fusion (data not shown). In the histological section of the five-week-old *Fgfr2*$^{S252W/+}$, there was bone tissue observed in the ventral part of the ISS (Figure 1p, black arrowheads), and the cartilage was protruding towards the intracranial space (Figure 1n). The SOS remained patent in both *Fgfr2*$^{S252W/+}$ mice and the littermate controls through the investigated period except for one *Fgfr2*$^{S252W/+}$ mouse (1/5) indicating the partial fusion (data not shown). However, the arrangement of chondrocytes in the SOS (the resting zone, the proliferating zone, and the hypertrophic zone), which was clearly recognized in the littermate controls (Figure 1q), seemed to be disturbed in the *Fgfr2*$^{S252W/+}$ (Figure 1r). We then investigated earlier stages, *Fgfr2*$^{S252W/+}$ mice demonstrated relatively normal ISS and SOS at P7 and P14. Although one *Fgfr2*$^{S252W/+}$ mouse (1/4) at P14 indicated minor protrusion and aberrant arrangement of the chondrocytes in the ISS (data not shown), almost all the histology did not show the difference between the mutants and the littermate controls (Figure 2c-f, i-l). All *Fgfr2c*$^{C342Y/+}$mice at three (3/3) and five weeks old (4/4) indicated the fused ISS (Figure 1k, l) while the littermate controls did not show the fusion (Figure 1i, j, white arrow). In the five-week-old *Fgfr2c*$^{C342Y/+}$, the ventral part of the ISS had bone tissue (Figure 1v, black arrowhead), and protrusion towards the brain side was also seen (Figure 1t), while the SOS maintained patency (Figure 1t, x). Histological sections revealed that *Fgfr2c*$^{C342Y/+}$ mice at P7 and P14 had protrusion of the ISS (Figure 2n, p, t, v), which was never seen in the littermate controls (Figure 2m, o, s, u). All the *Fgfr2c*$^{C342Y/+}$mice at P7 and P14 indicated normal SOS (Figure 2r, x). We previously reported that *Twist1*$^{+/-}$ mice do not demonstrate any fusion of the synchondroses until eight weeks old (Nuri et al., 2022). Similarly, our present study also indicated no fusion up to nine weeks old in *Twist1*$^{+/–}$ mice (data not shown).

3.2 Growth patterns of skull morphology of three CS mouse models after weaning

We next investigated growth pattern of skull morphology of the mouse models by geometric morphometric analysis (Klingenberg, 2010; Klingenberg, 2016) using the μCT images of skulls of each mouse model (*Fgfr2*$^{S252W/+}$, *Fgfr2c*$^{C342Y/+}$, and *Twist1*$^{+/-}$; Figure 1 b–d) from three to six or nine weeks old. 33 landmarks were placed on the reconstructed neurocranium of each mouse model in Avizo 6.3 by Isosurface function (Figure S1, Table S2), then growth pattern of skull morphology was assessed by landmark-based geometric morphometrics (Klingenberg, 2010; Klingenberg, 2016). CVA was applied to coordinates of the 33 landmarks

of each CS mouse model. Canonical variates provide linear combinations of the original variables that maximally separate *a priori* classified groups. In the present study, samples were classified according to the genotype and age prior to analyses. The detail of the sample size is shown in Table S1. Table 1 summarizes variance, correlation coefficient (r), and *p*-value corresponding to each CS model. CVA showed clear separation between CS model mice and their control littermates along CV1 (Figure 3−5, scatter plot). CV1 of $Fgfr2^{S252W/+}$, $Fgfr2c^{C342Y/+}$ and $Twist1^{+/-}$ accounted for 74.3%, 83.5% and 84.3% of the total shape variation, respectively (Table 1). CV2 of $Fgfr2^{S252W/+}$, $Fgfr2c^{C342Y/+}$, and $Twist1^{+/-}$ explained 14.1%, 10.5% and 9.43% of the total shape variation, respectively (Table 1). In $Fgfr2^{S252W/+}$and $Fgfr2c^{C342Y/+}$ mice, both CV1 and CV2 expressed the morphological changes with age, while only CV2 expressed the morphological changes in $Twist1^{+/-}$mice. The distribution of scores along CV3 of $Fgfr2^{S252W/+}$and $Fgfr2c^{C342Y/+}$ as well as their littermate controls overlapped regardless of age, they were not clearly separated (Figure S2, S3). CV1 scores and centroid sizes of individuals were positively correlated ($Fgfr2^{S252W/+}$: r = -0.866, $p < 0.0001$, $Fgfr2c^{C342Y/+}$: r = 0.903, $p < 0.0001$, $Twist1^{+/-}$: r = -0.772, $p < 0.0001$), while other CV scores except CV2 of $Twist1^{+/-}$ (r = 0.3320, $p < 0.0001$) did not show significant correlations to centroid sizes (Table 1). These results indicate that CV1 in each analysis summarizes size-correlated skull shape variation. In other words, the clear separation between each mouse model and the littermate controls along CV1 is partly due to their size differences.

$Fgfr2^{S252W/+}$ mice

The distribution of scores along CV1 was different between $Fgf2^{S252W/+}$ mice and their littermate controls. $Fgf2^{S252W/+}$ mice were mainly distributed in the positive area of CV1 and their littermate controls were localized in the negative area of CV1 (Figure 3, scatter plot). The wire frames with blue lines under the scatter plot indicate the morphological feature in negative/positive extreme of CV1, and those on the left side of the scatter plot are associated with CV2 (Figure 3, scatter plot). The morphological feature of $Fgf2^{S252W/+}$ mice exhibited taller and wider skull vaults (Figure 3, wireframes along the CV1 axis) relative to that of their littermate controls (Figure 3, wireframes along the CV1 axis). This brachycephalic phenotype was contributed by displacement of the frontal and parietal bones dorsally and bilateral expansion of the skull vault (Figure 3, wireframes along the CV1 axis). Furthermore, the facial area was greatly modified, the zygomatic arch shifted ventrally while the anterior part of the frontal process and the most anterior point of the first molar shifted dorsally (Figure 3, wireframes along the CV1 axis). Their growth trajectory was different from that of their littermate controls; the morphological changes with growth of $Fgf2^{S252W/+}$ mice were mainly indicated by CV2 rather than CV1, and the extent of change from three to nine weeks old along CV2 is greater in $Fgf2^{S252W/+}$ mice than littermate controls (Figure 3, scatter plot). The posterior region of the calvarium became more flattened along growth (Figure 3, wireframes along the CV2 axis), while the anteroventral extension of the facial area was relatively restricted in $Fgf2^{S252W/+}$ mice (Figure 3, wireframes along the CV1 axis).

$Fgfr2c^{C342Y/+}$ mice

The scores of *Fgfr2c*$^{C342Y/+}$ mice were distributed in the positive area of CV1 (Figure 4, scatter plot), they showed brachycephalic phenotypes similar to *Fgfr2*$^{S252W/+}$ mice (Figure 3–4, wireframes along the CV1 axis). The dorsal displacement of the parietal and interparietal bones mainly contributed to the morphological feature of *Fgfr2c*$^{C342Y/+}$ mice (Figure 4, wireframes along the CV1 axis). Furthermore, the posterior part of the skull vault, especially at the intersection of the temporal bone and the interparietal bone, showed marked expansion in width (Figure 4, wireframes along the CV1 axis). The foramen magnum of *Fgfr2c*$^{C342Y/+}$ mice was larger than that of their littermate controls (Figure 4, wireframes along the CV1 axis). In the facial area, they showed shorter zygomatic arch and the anterior displacement of the zygomatic process of the temporal bone (Figure 4, wireframes along the CV1 axis). The anterior part of the palate was shifted dorsally similar to *Fgfr2*$^{S252W/+}$ mice (Figure 3-4, wireframes along the CV1 axis). Ontogenic trajectory of *Fgfr2c*$^{C342Y/+}$ mice was similar to that of *Fgfr2*$^{S252W/+}$ mice, which is reflected in CV2 (Figure 3−4, scatter plot); the anterior region of the calvarium became more flattened along growth (Figure 4, wireframes along the CV2 axis), while the anteroventral extension of the facial area was relatively restricted (Figure 4, wireframes along the CV1 axis).

***Twist1*$^{+/-}$ mice**

We then investigated *Twist1*$^{+/-}$ mice that do not display fusion of the ISS but show coronal suture synostosis around the weaning period. The distribution of scores along CV1 was different between *Twist1*$^{+/-}$ mice and their wild-type littermates while scores of each age group were separated along CV2 (Figure 5, scatter plot). The scores of *Twist1*$^{+/-}$ mice were distributed in positive area of CV1 (Figure 5, scatter plot). *Twist1*$^{+/-}$ mice showed brachycephalic phenotype as seen in *Fgf2*$^{S252W/+}$ and *Fgfr2c*$^{C342Y/+}$ mice (Figure 3–5, wireframes along the CV1 axis). *Twist1*$^{+/-}$ mice were also characterized by the dysmorphogenesis of the zygomatic arch (Figure 5, wireframes along the CV1 axis). The zygomatic process of the temporal bone was shifted anteriorly, which was also observed in *Fgfr2c*$^{C342Y/+}$ mice (Figure 4–5, wireframes along the CV1 axis). On the other hand, ontogenetic trajectory of *Twist1*$^{+/-}$ mice was obviously different from those of *Fgf2*$^{S252W/+}$ and *Fgfr2c*$^{C342Y/+}$ mice (Figure 3−5, scatter plot). Both the littermate controls and *Twist1*$^{+/-}$ mice were plotted parallel to the CV2 axis, indicating that CV2 reflects the normal growth pattern of the littermate controls (Figure 5, scatter plot). Taking into account that CV2 scores and centroid sizes of individuals were positively correlated, the differences of the skull shape along CV2 axis are partly due to their sizes (Table 1). The calvarium becomes flattened and the facial area extends anteriorly with age (Figure 5, wireframes along the CV2 axis). While the trajectories along CV2 of *Twist1*$^{+/-}$ mice and the littermate controls were comparable, the extent of change is different. In particular, the extent from three to five weeks old was much greater in the littermate controls than *Twist1*$^{+/-}$ mice (Figure 5, scatter plot).

3.3 No obvious common features were detected among CS mouse models characterized by coronal suture fusion

Since the three CS mouse models share features of coronal suture synostosis in the early stage of their life and consequent skull dysmorphogenesis, we further investigated the extent that the fusion of the coronal suture

contributes to the skull shape using geometric morphometric analysis. The sample size of each group and the basic statistics of PCA are shown in Table 2. PC1 scores and centroid sizes of individuals were positively correlated ($r = 0.6986$, $p < 0.0001$) while other PC scores, excluding the PC3 score ($r = -0.6246$, $p < 0.0001$), did not show significant correlations to centroid sizes (Table 2). Despite the three CS mouse models being on different genetic backgrounds (*Fgfr2*$^{S252W/+}$ and *Twist1*$^{+/-}$ mice are on C57Bl/6J while *Fgfr2c*$^{C342Y/+}$ mice is on CD1), PC scores of the littermate controls of each model overlapped with each other (Figure 6). The PC scores of littermate controls and those of the three CS mutant mice separated along the PC1 axis. Considering PC1 scores and centroid sizes of individuals were positively correlated, the differences of PC scores of three CS mouse models and those of the littermate controls along the PC1 axis are partly due to their size differences (Table 2). Other PC scores of the three CS mouse models did not overlap each other along any PC axis (Figure S4). These results indicate that although the CS mouse models commonly show a brachycephalic phenotype, they do not have shared morphological features associated with coronal suture synostosis.

4. Discussion

Fgfr2$^{S252W/+}$, *Fgfr2c*$^{C342Y/+}$, and *Twist1*$^{+/-}$ mice have been used for revealing molecular mechanisms of syndromic CS and further understanding of the pathogenesis in CS patients (El Ghouzzi et al., 1997; Chen et al. 2003; Wang et al., 2005; Eswarakumar et al., 2004). In particular, the correlation between suture patency and craniofacial dysmorphology has been investigated by various strategies (Carver et al., 2002; Parsons et al., 2014; Motch Perrine et al., 2014). The growth pattern of the skull during perinatal stage by geometric morphometric analysis has been of long interests for researchers and clinicians working on craniosynostosis (Motch Perrine et al., 2014). However, long-term data of postnatal skull growth of CS mouse models have not yet been analyzed. To the best of our knowledge, the present study is the first report that investigated ontogenic trajectories of CS mouse models during fusion of the cranial synchondrosis and the coronal suture using a landmark-based geometric morphometric analysis of the skull. Furthermore, we examined whether coronal suture synostosis causes any shared morphological features among three CS mouse models.

The craniofacial growth pattern of *Fgfr2*$^{S252W/+}$ and *Fgfr2c*$^{C342Y/+}$ mice was successfully extracted using CVA. CV1 reflected the anteroventral extension of the facial area and flattening of calvaria while CV2 reflected the overall shape of the calvaria (Figure 3–4). The growth pattern of *Fgfr2*$^{S252W/+}$ and *Fgfr2c*$^{C342Y/+}$ mice was different from their littermate controls (Figure 3–4, scatter plot). The covariation among CV1 suggests that *Fgf2*$^{S252W/+}$ and *Fgfr2c*$^{C342Y/+}$ mice have difficulties in extending the facial area anteroventrally while their calvaria become flattened after weaning (Figure 3–4, wireframes along the CV1 and CV2 axis).

Considering the anatomical position and the role of craniofacial sutures and the synchondroses, it is reasonable to presume that the patency of facial sutures and the cranial synchondroses are key elements for the growth of the facial area. Purushothaman et al (2011) reports that neonatal *Fgf2*$^{S252W/+}$ mice with abnormal synostosis of facial sutures, such as premaxillary-maxillary suture and zygomatic arch, exhibit midface hypoplasia without fusion of cranial synchondroses. On the other hand, Pfeiffer syndrome patients, who carry autosomal dominant mutations in *FGFR1* or *FGFR2*, show strong correlation between midface hypoplasia and premature SOS closure (Paliga et al., 2014). Apert and Crouzon syndrome patients also show earlier fusion of the SOS (Mcgrath et al., 2012; Tahiri et al., 2014). Although early ossification of the ISS in *Fgfr2c*$^{C342Y/+}$ and *Fgfr2*$^{P253R/+}$ mice has been reported (Liu et al., 2013; Yin et al., 2008; Moazen et al., 2022), the detail in *Fgfr2*$^{S252W/+}$ mice has not been sufficiently studied. In this study, we identified fusion of the ISS in *Fgfr2*$^{S252W/+}$ mice occurs later than three weeks old (Figure 1–2), as seen in *Fgfr2c*$^{C342Y/+}$ mice (Eswarakumar et al., 2004; Liu et al., 2013, this study). Of contrast, *Twist1*$^{+/-}$ mice maintain patency of the ISS and show the similar facial growth to the littermate controls (Figure 5, wireframes along the CV2 axis).

The fusion process of the cranial synchondroses in the mutants remains to be elucidated. Among the *Fgfr2* mRNA isoforms, *Fgfr2b* and *Fgfr2c* are transcribed in the perichondria, and the proliferative and the resting zone of the chondrocytes in the cranial base (Rice et al., 2003). A recent study showed that expression of

Fgfr2 with an Apert mutation in chondrocytes accelerates maturation and hypertrophy of the chondrocytes, resulting in ossification of the synchondroses in the cranial base (Nagata et al., 2011). The ossification wave seems to break into the SOS from the edges of bone forming region of the sphenoid or the occipital bones (Nagata et al., 2011). In our study, we observed the bone at the ventral side of the ISS bridging the presphenoid and the basisphenoid bones in *Fgfr2*$^{S252W/+}$ and *Fgfr2c*$^{C342Y/+}$ mice (Figure 1). These observations are consistent with the finding that the secondary ossification center is absent in the cranial base (Wei et al., 2016). We found that a few *Fgfr2* mutant mice at P7 and P14 demonstrated protrusion of the ISS without mineralization. These ISS exhibited slight aberrant arrangement of chondrocytes (Figure 2p, v). Therefore, it is possible that a primary defect of chondrocytes in the ISS induced morphological disturbance of cartilage in the *Fgfr*2 mutant mice. In addition, the chondrocyte morphology may be further exacerbated by the pressure resulting from ossification of the ventral side of the ISS. Another possibility is that the pressure induced by the fusion of the facial sutures in *Fgfr2*$^{S252W/+}$ and *Fgfr2c*$^{C342Y/+}$ mice (Purushothaman et al., 2011: Motch Perrine et al., 2014; Martinez-Abadias et al. 2013) brought the mechanical force resulting in protrusion and disturbed morphology of chondrocytes in the ISS of *Fgfr*2 mutant mice.

Fgfr2$^{S252W/+}$ mice are previously shown to have the fusion of sutures in the zygomatic-maxillary, premax-maxillary, and fronto-maxillary bones at P0 (Purushothaman et al., 2011; Motch Perrine et al., 2014). Some of *Fgfr2c*$^{C342Y/+}$ mice also show fusion of the zygomatic-maxillary bones (Martinez-Abadias et al. 2013). Furthermore, in neonatal *Fgfr2*$^{S252W/+}$ mice, the angle of the presphenoid to the horizon plane is larger than that in control mice, and the anterior part of the presphenoid bone in *Fgfr2*$^{S252W/+}$ mice raises up the premaxilla bone (Kim et al., 2020; Martinez-Abadias et al., 2010), which was presumed to result from an increased intracranial pressure (Kreiborg et al. 1993; Connolly et al. 2004). Those premature fusion of the facial sutures and dysmorphology of the cranial base precedes the fusion of the ISS. Therefore, these factors may also contribute to the characteristics of craniofacial morphology of the mutant mice detected in this study. However, since the length of the cranial base continues to grow until around eight weeks old in normal condition (Vora et al., 2015), the fusion of the ISS, occurring around three weeks of age in the mutants, could contribute to the midface hypoplasia at least after this age, which is indicated by CV1 and CV2 in this study (Figure 3–4).

To our surprise, *Twist1*$^{+/-}$ mice showed a similar growth pattern to that of littermate controls contrary to the *Fgfr2* mutant mice. Our data demonstrated that growth pattern of the skull shape (CV2 in Figure 5) is not largely affected by the synostosis of the coronal suture. Both *Twist1*$^{+/-}$ mice and their littermate controls continue to grow into a more flattened calvarium and anteriorly extended the facial area (Figure 5, wireframes along the CV2 axis). *Twist1* plays an important role in mesenchymal cell fate, especially in differentiation from mesenchymal stem cells into osteoblasts, chondrocytes, or adipocytes (Miraoui and Marie, 2010) and functions in maintenance of the suture through regulation of FGFR2 and RUNX2 (Johnson et al., 2000; Connerney et al., 2006). Furthermore, *Twist1* regulates proliferation, differentiation and cell death of osteoblasts (Miraoui and Marie, 2010). It has been suggested that the growth of the brain affects skull

morphology and vice versa through developmentally indispensable signaling (Hill et al., 2013; Richtsmeier and Flaherty, 2013). Yu et al. (2021) reported that regeneration of the coronal suture at P14 leads to a normalized skull shape, intracranial pressure, and cognitive function to *Twist1*$^{+/-}$ mice, indicating that the growth of the brain is potentially normal in *Twist1*$^{+/-}$ mice. In contrast, *Fgfr2* is expressed in developing brain (Wilke et al., 1997), and the skull growth of the *Fgfr2*$^{S252W/+}$ and the *Fgfr2c*$^{C342Y/+}$ mice seems to be affected by brain (Motch Perrine et al., 2017). Of note, timing of the morphological change of *Twist1*$^{+/-}$ mice was different from that of the littermate controls (Figure 5, scatter plot). The relative skull height of the littermate controls gradually decreases, which is consistent with the previous report (Wei et al., 2017). In contrast, *Twist1*$^{+/-}$ mice exhibit accelerated growth in the skull height until three weeks old (Nuri et al., 2022), and the skull then rapidly flattened by five weeks old (Figure 5, scatter plot and wireframes along the CV2 axis), probably due to the synostosis of the coronal suture at early stage. Based on these data, although the growth pattern of the skull shape in *Twist1*$^{+/-}$ mice is relatively similar to that in littermate controls, the fusion of the coronal suture seems to delay the change of skull growth pattern in *Twist1*$^{+/-}$ mice. In other words, *Twist1* has an important role in the early phase of skull development, while abnormalities in the skull of *Twist1*$^{+/-}$ mice after weaning is attributed to the premature fusion of the coronal suture, but not decreased function of this gene. Although the expression of *Twist1* in mouse embryos and fetuses is detected in many tissues (Bourgeois et al., 1998; Barnes and Firulli, 2009), it is not clear whether this gene is expressed in craniofacial regions including the brain during the postnatal period. These data may give some insights into the role of *Twist1* after birth and the treatment plan for Saethre–Chotzen syndrome patients.

In the suture mesenchyme, the TWIST1 homodimer functions as a FGFR2 agonist in cells of the osteogenic front while the TWIST1 heterodimer acts as an antagonist of FGFR2 (Connerney et al., 2006) and downregulates BMP signaling, which are downstream of the FGFR2 signaling pathway (Connerney et al., 2008). However, in the cranial base, the role of *Twist1* has been elusive. *Twist1*$^{+/-}$ mice showed accelerated tether thickening at the SOS between P25 and P30 compared to the control mice while thickness, but volume and tether number of the SOS was not different from the control (Hermann et al., 2012). In addition, *Twist1*$^{+/-}$ mice have no fusion in the ISS and the SOS until nine weeks old (Nuri et al., 2022, this study). *Twist1*$^{+/-}$ mice and *Fgfr2* mutant mice decisively differ in the growth pattern of the skull, which is mainly at the facial area, and the difference seems to be partially caused by fusion of the ISS of the cranial base.

We also tried to detect shared morphological features among three CS mouse models based on coronal suture fusion. The brachycephalic phenotype characterized by higher, wider, and shorter dimensions in the anteroposterior direction of the neurocranium was found by the wireframes, indicating morphological features of those CS mouse models, in common (Figure 3–5, wireframes along the CV1 axis). This phenotype is consistent with prenatal and postnatal CS models (El Ghouzzi et al., 1997; Parsons et al., 2014; Martinez-Abadias et al., 2010; Wang et al., 2005; Eswarakumar et al., 2004; Marghoub et al., 2018) and CS patients of Saethre–Chotzen, Apert, and Crouzon syndromes (Flaherty et al., 2016). However, strict overlaps of distribution on CS mouse models were not detected by PCA for all CS models (Figure 6, Figure S4) while the

distribution of each littermate control group of the three CS mouse models being on different genetic backgrounds (*Fgfr2*$^{S252W/+}$ and *Twist1*$^{+/-}$ mice are on C57Bl/6J while *Fgfr2c*$^{C342Y/+}$ mice is on CD1) were overlapped each other (Figure 6). These results obtained by geometric morphometric analysis indicate that although these CS mouse models commonly show a brachycephalic phenotype, they do not have other shared features. These data corroborate the previous reports which suggest that craniofacial dysmorphology found in CS mouse models is not induced simply by early fusion of the coronal suture (Nagata et al.,2011; Martinez-Abadias et al., 2010; Parsons et al., 2014). Considering that *Twist1* and *Fgfr2* regulate not only the coronal suture but also patency of other sutures (Connerney et al., 2008; Motch Perrine et al., 2014; Martinez-Abadias et al., 2013) and various biological phenomenon (Miraoui and Marie, 2010; Ornitz and Itoh, 2015; Peskett et al., 2017), it is reasonable to think that an orchestration of those functions brings craniofacial dysmorphology.

In this study, we analyzed ontogenic trajectories after weaning in three syndromic CS mouse models using geometric morphometrics. Our main finding is that the skull base phenotype, which occur after loss of patency in coronal and facial sutures, contributes to the craniofacial phenotype progression in *Fgfr*2 mutant mice. The detailed characterization of morphological changes in a long-term period can provide the fundamental information for revealing the pathogenic progression and improving treatment of syndromic CS patients.

Acknowledgments

We appreciate Jin Cheng-Xue for his technical support. We also thank Michael Fagan and Christian Babbs for assistance with collection and scanning of *Fgfr2*$^{C342Y/+}$ mice.

Authors contribution

This project was conceived by S.I., M.T., Y.N. and T.N. The data collection of μCT scanning images of *Fgfr2*$^{S252W/+}$ and *Twist1*$^{+/-}$ mice was performed by Y.H., M.T. and T.N. Images of *Fgfr2*$^{C342Y/+}$ mice were collected and scanned by M.M. and E.P. Geomorphometric analysis was performed by M.T., D.K. and Y.H. Sample preparation for histological analysis of *Fgfr2*$^{S252W/+}$mice was carried out by Y.H. and T.F., and that of *Fgfr2*$^{C342Y/+}$ mice was performed by M.S. and E.P. Y.H., M.T. and S.I. drafted the manuscript. All authors contributed to critical revision of the manuscript and approval of the article.

Conflict of interest

The authors declare no competing or financial interests.

Funding

This work was supported by grants-in-aid from: Ministry of Education, Culture, Sports, Science, and Technology of Japan [18K06821 to M.T., 18K19605 and 21H03098 to S.I.], Royal Academy of Engineering (10216/119 to MM), Engineering and Physical Science Research Council (EP/W008092/1 to MM), Newlife, the charity for disabled children (award 17-18/18 to EP) and by the NIHR Great Ormond Street Hospital Biomedical Research Centre. The views expressed are those of the author(s) and not necessarily those of the NHS, the NIHR or the Department of Health.

Data Availability

The data that support the findings of this study are available from the corresponding author upon reasonable request.

References

Adams, D. C., Rohlf, F. J., & Slice, D. E. (2004). Geometric morphometrics: Ten years of progress following the 'revolution'. *Ital J Zool.* **71**, 5–16.

Barnes, R. M., & Firulli, A. B. (2009). A twist of insight - the role of Twist-family bHLH factors in development. *Int. J. Dev. Biol*. ***53*(7)**, 909–924.

Beederman, M., Farina, E. M., & Reid, R. R. (2014). Molecular basis of cranial suture biology and disease: Osteoblastic and osteoclastic perspectives. *Genes Dis.* ***1*(1)**, 120–125.

Boulet, S. L., Rasmussen, S. A., & Honein, M. A. (2008). A population-based study of craniosynostosis in metropolitan Atlanta, 1989-2003. *Am j Med Genet A.****146A*(8)**, 984–991

Bourgeois, P., Bolcato-Bellemin, A. L., Danse, J. M. et al. (1998). The variable expressivity and incomplete penetrance of the twist-null heterozygous mouse phenotype resemble those of human Saethre-Chotzen syndrome. *Hum. Mol. Genet*. ***7*(6)**, 945–957.

Breakey, R. W. F., Knoops, P. G. M., Borghi, A. et al. (2018). Intracranial Volume and Head Circumference in Children with Unoperated Syndromic Craniosynostosis. *Plast. Reconstr. Surg.* **142**, 708e-717e.

Carver, E. A., Oram, K. F., & Gridley, T. (2002). Craniosynostosis in Twist heterozygous mice: a model for Saethre-Chotzen syndrome. *Anat Rec (Hoboken).* **268(2)**, 90-92.

Cendekiawan T., Wong RW., & Rabie AB. (2010). Relationships between cranial base synchondroses and craniofacial development: A review. *Open Anat J.* **2**, 67–75.

Chen, L., Li, D., Li, C., Engel, A., & Deng, C. X. (2003). A Ser252Trp [corrected] substitution in mouse fibroblast growth factor receptor 2 (Fgfr2) results in craniosynostosis. *Bone*. **33(2)**, 169–178.

Chen, Z. F., & Behringer, R. R. (1995). Twist is required in head mesenchyme for cranial neural tube morphogenesis. *Genes Dev.* **9(6)**, 686-699.

Cohen MM Jr. (2005). Editorial: perspectives on craniosynostosis. *Am J Med Genet A.* 1**36 A (4)**, 313-326.

Connerney, J., Andreeva, V., Leshem, Y., Muentener, C. et al. (2006). Twist1 dimer selection regulates cranial suture patterning and fusion. *Dev Dyn.****235*(5)**, 1345–1357.

Connerney, J., Andreeva, V., Leshem, Y. et al. (2008). Twist1 homodimers enhance FGF responsiveness of the cranial sutures and promote suture closure. *Dev. Bio.* **318(2)**, 323–334.

Connolly, JP., Gruss, J., Seto, ML. et al. (2004). Progressive postnatal craniosynostosis and increased intracranial pressure. *Plast. Reconstr. Surg*. **113(5)**, 1313–1323.

El Ghouzzi, V., Le Merrer, M., Perrin-Schmitt, F. et al. (1997). Mutations of the TWIST gene in the Saethre-Chotzen syndrome. *Nat Genet*. **15(1)**, 42-46

Eswarakumar, V. P., Horowitz, M. C., Locklin, R., Morriss-Kay, G. M., & Lonai, P. (2004). A gain-of-function mutation of Fgfr2c demonstrates the roles of this receptor variant in osteogenesis. *Proc. Natl. Acad. Sci. USA.**101***(34)**, 12555–12560.

Fenwick, A. L., Goos, J. A., Rankin, J. et al. (2014). Apparently synonymous substitutions in FGFR2 affect splicing and result in mild Crouzon syndrome. *BMC medical genet.* ***15,*** 95.

Flaherty, K., Singh, N., & Richtsmeier, J. T. (2016). Understanding craniosynostosis as a growth disorder. *Dev Bio*. ***5*(4)**, 429–459.

Hayashi I. (2003). Morphological relationship between the cranial base and dentofacial complex obtained by reconstructive computer tomographic images. *Eur J Orthod*. ***25*(4)**, 385–391.

Hermann, C. D., Lee, C. S., Gadepalli, S.et al. (2012). Interrelationship of cranial suture fusion, basicranial development, and resynostosis following suturectomy in twist1(+/-) mice, a murine model of Saethre-Chotzen syndrome. *Calcif. Tissue Int*. ***91*(4)**, 255–266.

Hill, C. A., Martínez-Abadías, N., Motch, S. M. et al. (2013). Postnatal brain and skull growth in an Apert syndrome mouse model. *Am J Med Genet C Semin Med Genet.* Part A, **161A(4)**, 745–757.

Ibrahimi, O. A., Eliseenkova, A. V., Plotnikov, A. N.et al. (2001). Structural basis for fibroblast growth factor receptor 2 activation in Apert syndrome. *Proc. Natl. Acad. Sci USA.* **98(13)**,7182-7.

Johnson, D., Iseki, S., Wilkie, A. O., & Morriss-Kay, G. M. (2000). Expression patterns of Twist and Fgfr1, -2 and -3 in the developing mouse coronal suture suggest a key role for twist in suture initiation and biogenesis. *Mechanisms of development*, **91(1-2)**, 341–345.

Kawai, S., Takagi, Y., Kaneko, S., & Kurosawa, T. (2011). Effect of three types of mixed anesthetic agents alternate to ketamine in mice. *Exp anim.**60***(5)**, 481–487.

Kim, B., Shin, H., Kim, W.et al. (2020). PIN1 Attenuation Improves Midface Hypoplasia in a Mouse Model of Apert Syndrome. *J. Dent. Res*. ***99*(2)**, 223–232.

Klingenberg, C. (2010). Evolution and development of shape: integrating quantitative approaches. *Nat Rev Genet.* **11**, 623–635.

Klingenberg C. P. (2011). MorphoJ: an integrated software package for geometric morphometrics. *Mol Ecol Resour*.***11*(2)**, 353–357.

Klingenberg C. P. (2016). Size, shape, and form: concepts of allometry in geometric morphometrics. *Dev. Genes Evol*.**226(3)**, 113–137.

Kreiborg, S., Marsh, JL., Cohen, MM. et al. (1993). Comparative three-dimensional analysis of CT-scans of the calvaria and cranial base in Apert and Crouzon syndromes. *J Craniomaxillofac Surg*. **21(5)**, 181–188.

Krishan, K., & Kanchan, T. (2013). Evaluation of spheno-occipital synchondrosis: A review of literature and considerations from forensic anthropologic point of view. *J. Forensic Dent. Sci*. ***5*(2)**, 72–76.

Lance, S., & Governale, M.D. (2015). Craniosynostosis. *Pediatr Neurol*. **53(5)**, 394-401.

Lee, K., Stanier, P., & Pauws, E. (2019). Mouse Models of Syndromic Craniosynostosis. *Mol Syndromol*. ***10*(1-2)**, 58–73.

Libby, J., Marghoub, A., Johnson, D. et al. (2017). Modelling human skull growth: a validated computational model. *J R Soc Interface*. ***14*(130)**, 20170202

Liu, J., Nam, H.K., & Wang, E.（2013）. Further Analysis of the Crouzon Mouse: Effects of the FGFR2^{C342Y}Mutation Are Cranial Bone–Dependent. *Calcif Tissue Int.* **92**, 451–466.

Madeline, LA., & Elster. AD. (1995) Postnatal development of the central skull base: normal variants. Radiology. **196(3)**, 757-63.

Marghoub, A., Libby, J., Babbs, C. et al. (2018). Predicting calvarial growth in normal and craniosynostotic mice using a computational approach. *J. Anat.* **232**, 440-448.

Martínez-Abadías, N., Percival, C., Aldridge, K. et al. (2010). Beyond the closed suture in apert syndrome mouse models: evidence of primary effects of FGFR2 signaling on facial shape at birth. *Dev.Dyn.**239***(11), 3058–3071.

Martínez-Abadías, N., Motch, S. M., Pankratz, T. L. et al. (2013). Tissue-specific responses to aberrant FGF signaling in complex head phenotypes. *Dev. Dyn.**242***(1), 80–94.

McGrath, J., Gerety, P. A., Derderian, C. A. et al. (2012). Differential closure of the spheno-occipital synchondrosis in syndromic craniosynostosis. *Plast. Reconstr. Surg*. **130(5)**, 681e–689e.

Miraoui, H., & Marie, P. J. (2010). Pivotal role of Twist in skeletal biology and pathology. *Gene. **468***(1-2), 1–7.

Moazen, M., Hejazi, M., Savery, D. et al. (2022). Mechanical loading of cranial joints minimizes the craniofacial phenotype in Crouzon syndrome. *Sci. Rep*. ***12***(1), 9693.

Motch Perrine, S. M., Cole, T. M., 3rd, Martínez-Abadías, N.et al. (2014). Craniofacial divergence by distinct prenatal growth patterns in Fgfr2 mutant mice. *BMC Dev. Biol. **14,*** 8.

Motch Perrine, S. M., Stecko, T., Neuberger, T. et al. (2017). Integration of Brain and Skull in Prenatal Mouse Models of Apert and Crouzon Syndromes. *Front. Hum. Neurosci. **11***, 369.

Nagata, M., Nuckolls, G. H., Wang, X. et al. (2011). The primary site of the acrocephalic feature in Apert Syndrome is a dwarf cranial base with accelerated chondrocytic differentiation due to aberrant activation of the FGFR2 signaling. *Bone*. **48(4)**, 847–856.

Nuri, T., Ota, M., Ueda, K., & Iseki, S. (2022). Quantitative Morphologic Analysis of Cranial Vault in Twist1+/- Mice: Implications in Craniosynostosis. *Plast. Reconst. Surg*. **149(1)**, 28e–37e.

Opperman L.A. (2000). Cranial sutures as intramembranous bone growth sites. *Dev. Dyn.* **219**, 472– 485

Ornitz, D. M., & Marie, P. J. (2002). FGF signaling pathways in endochondral and intramembranous bone development and human genetic disease. *Genes Dev.***16(12)**, 1446-1465.

Ornitz, D. M., & Itoh, N. (2015). The Fibroblast Growth Factor signaling pathway. *Dev Bio. **4***(3), 215–266.

Paliga, J. T., Goldstein, J. A., Vossough, A., Bartlett, S. P., & Taylor, J. A. (2014). Premature closure of the spheno-occipital synchondrosis in Pfeiffer syndrome: a link to midface hypoplasia. *J. Craniofac. Surg.* ***25*****(1)**, 202–205.

Parsons, T. E., Weinberg, S. M., Khaksarfard, K. et al. (2014). Craniofacial shape variation in Twist1+/- mutant mice. *Anat Rec (Hoboken).* **297(5)**, 826-833.

Paznekas, W. A., Cunningham, M. L., Howard, T. D. et al. (1998). Genetic heterogeneity of Saethre-Chotzen syndrome, due to TWIST and FGFR mutations. *Am J Hum Genet.* **62(6)**, 1 370-1380

Peskett, E., Kumar, S., Baird, W. et al. (2017). Analysis of the *Fgfr2*^{C342Y} mouse model shows condensation defects due to misregulation of *Sox9* expression in prechondrocytic mesenchyme. *Biology open*. ***6*****(2)**, 223–231.

Plotnikov, A. N., Hubbard, S. R., Schlessinger, J., & Mohammadi, M. (2000). Crystal structures of two FGF-FGFR complexes reveal the determinants of ligand-receptor specificity. *Cell*, **101(4)**, 413–424.

Purushothaman, R., Cox, T. C., Maga, A. M., & Cunningham, M. L. (2011). Facial suture synostosis of newborn Fgfr1(P250R/+) and Fgfr2(S252W/+) mouse models of Pfeiffer and Apert syndromes. *Birth defects research*. **91(7),** 603–609.

Rice, D. P., Rice, R., & Thesleff, I. (2003). Fgfr mRNA isoforms in craniofacial bone development. *Bone*, ***33*****(1)**, 14–27.

Richtsmeier, J.T., & Flaherty, K. (2013). Hand in glove: brain and skull in development and dysmorphogenesis. *Acta Neuropathol.***125**, 469–489.

Slater, B. J., Lenton, K. A., Kwan, M. D. et al. (2008). Cranial sutures: a brief review. *Plast. Reconstr. Surg.****121*****(4)**,170e–178e.

Tahiri, Y., Paliga, J. T., Vossough, A., Bartlett, S. P., & Taylor, J. A. (2014). The spheno-occipital synchondrosis fuses prematurely in patients with Crouzon syndrome and midface hypoplasia compared with age- and gender-matched controls. *J. Oral Maxillofac. Surg.****72*****(6)**, 1173–1179.

Vora, S. R., Camci, E. D., & Cox, T. C. (2016). Postnatal Ontogeny of the Cranial Base and Craniofacial Skeleton in Male C57BL/6J Mice: A Reference Standard for Quantitative Analysis. *Frontiers in physiology*, **6**, 417.

Wang, Y., Xiao, R., Yang, F. et al. (2005). Abnormalities in cartilage and bone development in the Apert syndrome FGFR2(+/S252W) mouse. *Development.***132(15)**, 3537-3548.

Wei, X., Hu, M., Mishina, Y., & Liu, F. (2016). Developmental Regulation of the Growth Plate and Cranial Synchondrosis. *Journal of dental research*, **95(11)**, 1221–1229.

Wei, X., Thomas, N., Hatch, N. E., Hu, M., & Liu, F. (2017). Postnatal Craniofacial Skeletal Development of Female C57BL/6NCrl Mice. *Front Physiol.***8**, 697.

Wilkie, A. O., Slaney, S. F., Oldridge, M. et al. (1995). Apert syndrome results from localized mutations of FGFR2 and is allelic with Crouzon syndrome. *Nat Genet*.**9(2)**, 1 65-72.

Wilke, T. A., Gubbels, S., Schwartz, J., & Richman, J. M. (1997). Expression of fibroblast growth factor receptors (FGFR1, FGFR2, FGFR3) in the developing head and face. *Dev. Dyn.* **210(1)**, 41–52.

Yin, L., Du, X., Li, C. et al. (2008). A Pro253Arg mutation in fibroblast growth factor receptor 2 (Fgfr2) causes skeleton malformation mimicking human Apert syndrome by affecting both chondrogenesis and osteogenesis. *Bone.* ***42*****(4)**, 631–643.

Yu, M., Ma, L., Yuan, Y. et al. (2021). Cranial Suture Regeneration Mitigates Skull and Neurocognitive Defects in Craniosynostosis. *Cell.* ***184*****(1)**, 243–256.

Figure.1

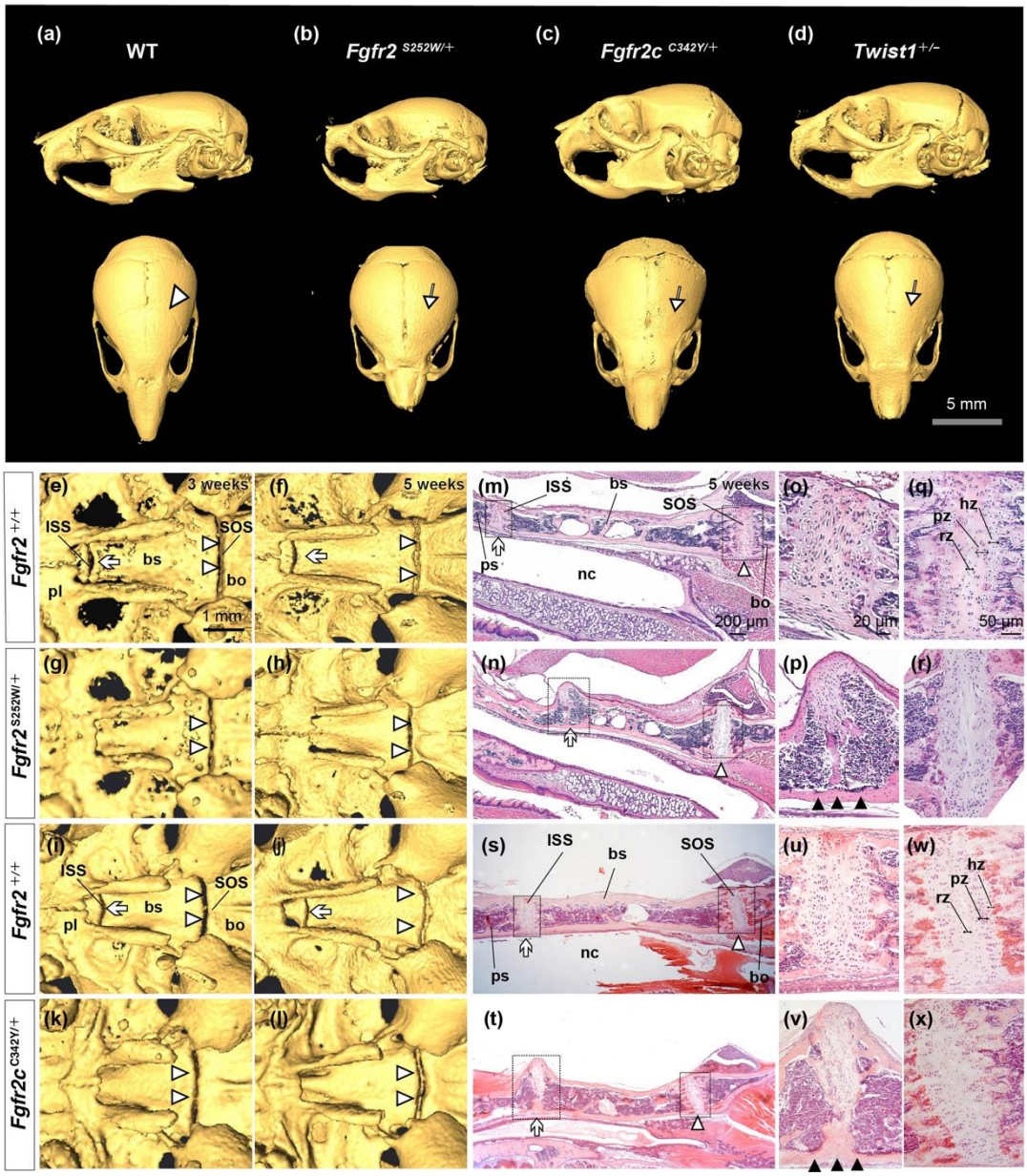
(a) WT
(b) Fgfr2 S252W/+
(c) Fgfr2c C342Y/+
(d) Twist1+/-
5 mm
Fgfr2 +/+
Fgfr2 S252W/+
Fgfr2 +/+
Fgfr2c C342Y/+
(e) 3 weeks
(f) 5 weeks
(m) 5 weeks
ISS
SOS
bs
pl
bo
ps
nc
1 mm
200 μm
20 μm
50 μm
hz
pz
rz

Figure.2

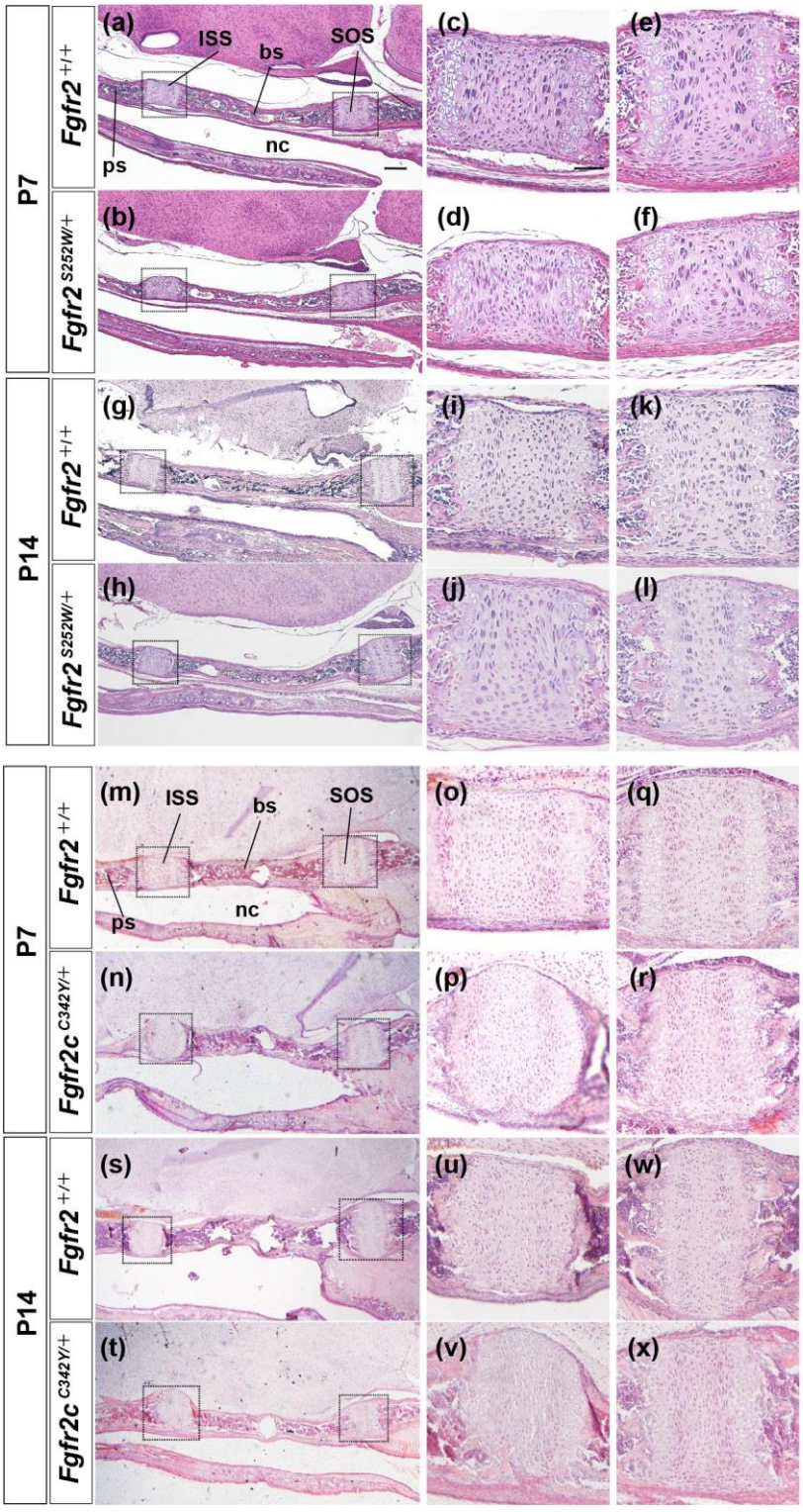
P7
P14
Fgfr2 +/+
Fgfr2 S252W/+
Fgfr2c C342Y/+
(a)
(b)
(c)
(d)
(e)
(f)
(g)
(h)
(i)
(j)
(k)
(l)
(m)
(n)
(o)
(p)
(q)
(r)
(s)
(t)
(u)
(v)
(w)
(x)
ISS
bs
SOS
nc
ps

Figure.3

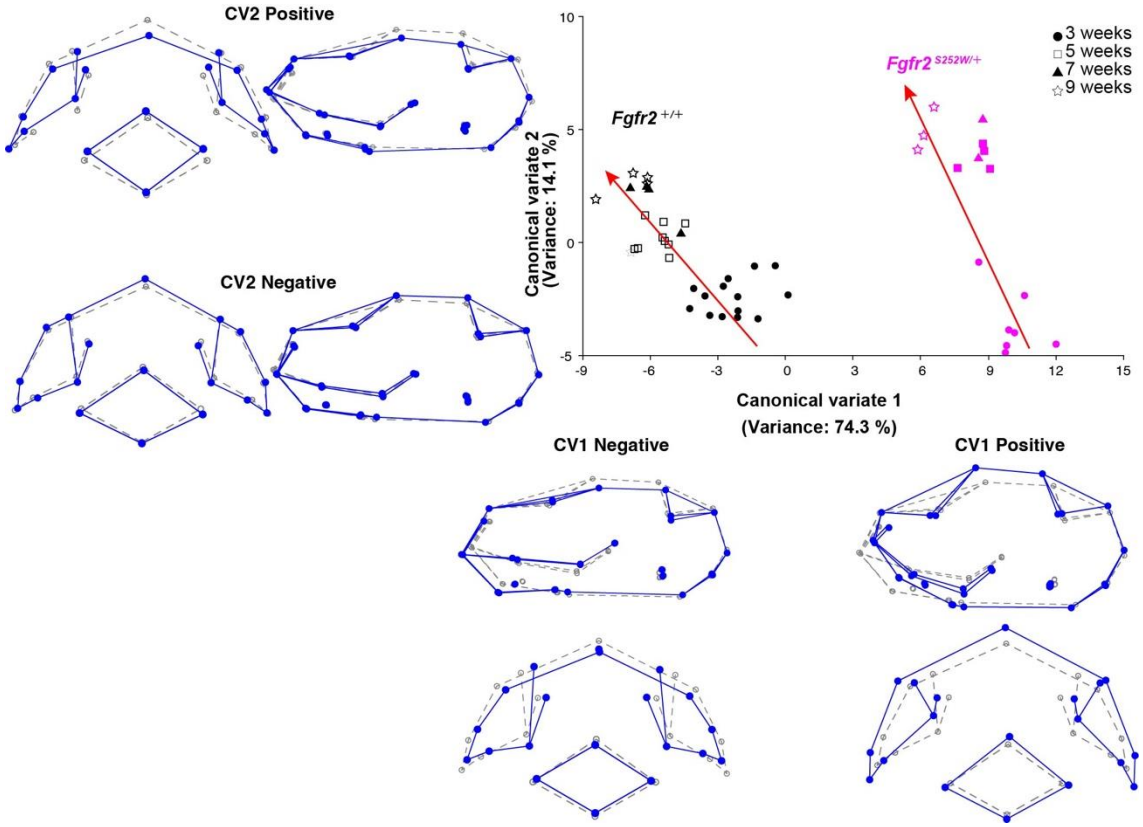
CV2 Positive
CV2 Negative
Canonical variate 2
(Variance: 14.1 %)
Canonical variate 1
(Variance: 74.3 %)
Fgfr2 +/+
Fgfr2 S252W/+
3 weeks
5 weeks
7 weeks
9 weeks
CV1 Negative
CV1 Positive

Figure.4

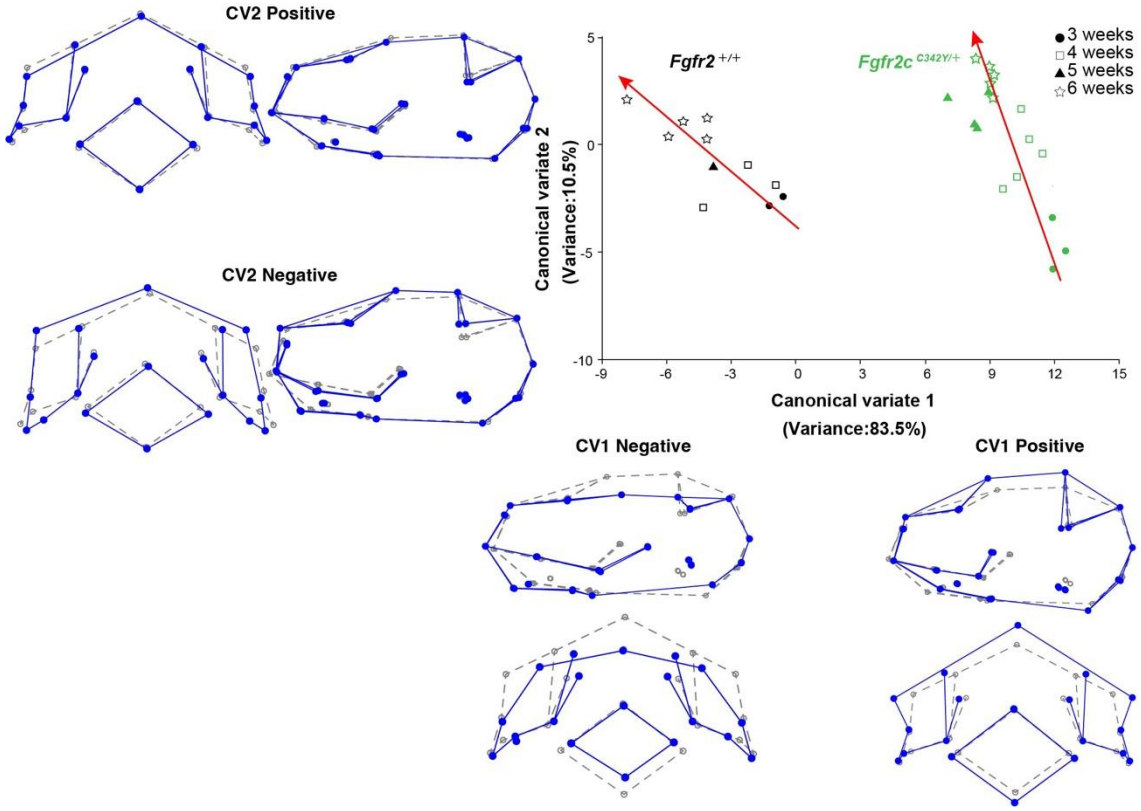
CV2 Positive
CV2 Negative
Fgfr2 +/+
Fgfr2c C342Y/+
3 weeks
4 weeks
5 weeks
6 weeks
Canonical variate 2
(Variance:10.5%)
Canonical variate 1
(Variance:83.5%)
CV1 Negative
CV1 Positive

Figure.5

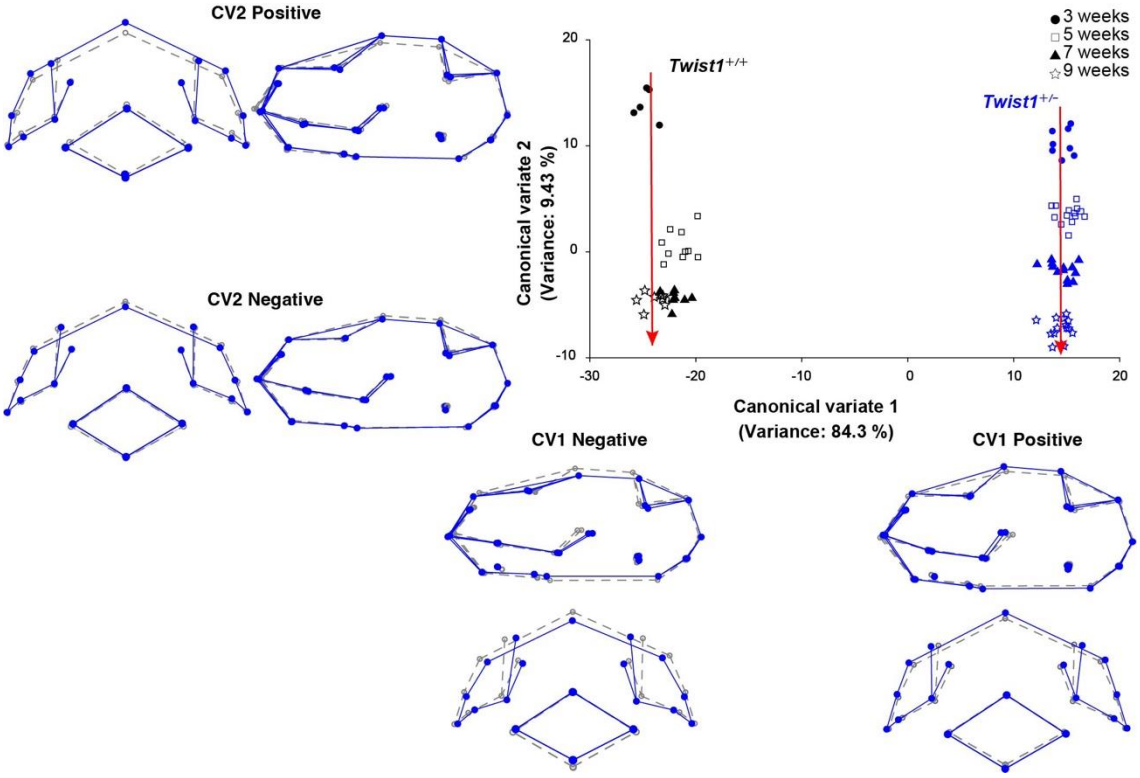
CV2 Positive
CV2 Negative
3 weeks
5 weeks
7 weeks
9 weeks
Twist1+/+
Twist1+/-
Canonical variate 2
(Variance: 9.43 %)
Canonical variate 1
(Variance: 84.3 %)
CV1 Negative
CV1 Positive

Figure.6

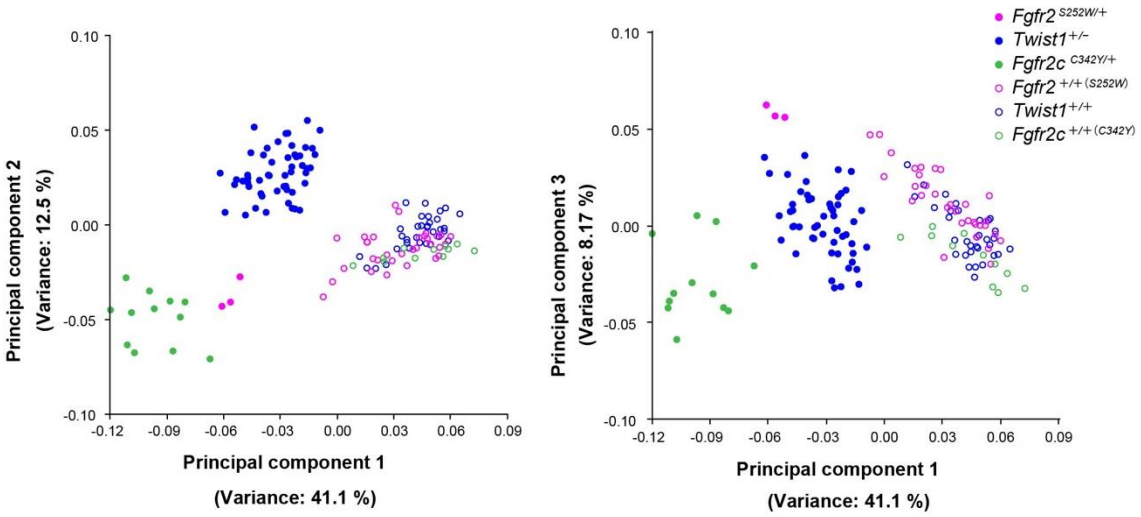
Principal component 2
(Variance: 12.5 %)
Principal component 1
(Variance: 41.1 %)
Principal component 3
(Variance: 8.17 %)
Principal component 1
(Variance: 41.1 %)
Fgfr2 S252W/+
Twist1 +/−
Fgfr2c C342Y/+
Fgfr2 +/+ (S252W)
Twist1 +/+
Fgfr2c +/+ (C342Y)

Table 1 Results of CVA analysis for each three craniosynostosis mouse model

***Fgfr2*$^{S252W/+}$**	**PCx**	**CV1**	**CV2**	**CV3**	**CV4**
	Variance (%)	74.3	14.1	4.91	2.96
	Correlation coefficient(r)	-0.866	0.355	0.125	-0.109
	***P*-value**	**<0.0001**	0.013	0.396	0.460
Fgfr2c $^{C342Y/+}$	**PCx**	**CV1**	**CV2**	**CV3**	**CV4**
	Variance (%)	83.5	10.5	3.18	1.60
	Correlation coefficient(r)	0.903	0.357	0.022	-0.004
	***P*-value**	**<0.0001**	0.062	0.910	0.985
***Twist1*$^{+/-}$**	**PCx**	**CV1**	**CV2**	**CV3**	
	Variance (%)	84.3	9.43	2.66	
	Correlation coefficient(r)	-0.772	-0.481	-0.130	
	***P*-value**	**<0.0001**	**<0.0001**	0.238	

Table 2 Sample size and result of PCA analysis for three craniosynostosis mouse models

Sample size	PCx	PC1	PC2	PC3	PC4	PC5	PC6
	Variance (%)	41.1	12.5	8.17	4.42	3.01	2.89
Fgfr2$^{S252W/+}$: 3 *Fgfr2*$^{+/+(S252W)}$: 32 *Fgfr2c*$^{+/C342Y}$: 12 *Fgfr2c*$^{+/+(C342Y)}$: 11 *Twist1*$^{+/}$*:* 52 *Twist1*$^{+/+}$: 33	**Correlation coefficient (r)**	0.699	-0.081	-0.625	0.001	-0.020	-0.069
	***P*-value**	**<0.0001**	0.334	**<0.0001**	0.991	0.812	0.412

Figure legends

Figure 1. 3D reconstructions of the skull in craniosynostosis mouse models at three weeks old and the cranial base in *Fgfr2*$^{S252W/+}$ mice and *Fgfr2c*$^{C342Y/+}$ mice at three and five weeks old.

Left lateral (top) and superior (bottom) views of wild type (a), *Fgfr2*$^{S252W/+}$ Apert syndrome mouse model (b), *Fgfr2c*$^{C342Y/+}$ Crouzon syndrome mouse model (c), and *Twist1*$^{+/-}$ Seathre-Chotzen syndrome mouse model (d), respectively. Fusion of the coronal suture is apparent in each CS mouse model (white arrows in b–d) whereas the coronal suture of the wild-type mouse keeps patency (white arrowhead in a).

(e–l) 3D reconstructions of μCT images of cranial base at three (e, g, i, k) and five weeks old (f, h, j, l) of littermate controls of *Fgfr2*$^{S252W/+}$ mice (e, f), *Fgfr2*$^{S252W/+}$ mice (g, h), littermate controls of *Fgfr2c*$^{C342Y/+}$ mice (i, j) and *Fgfr2c*$^{C342Y/+}$ mice (k, l). White arrows and white arrowheads indicate the inter-sphenoid synchondrosis (ISS) and the sphenoid-occipital synchondrosis (SOS), respectively. (m–x) Hematoxylin-Eosin staining of sagittal sections of the cranial base at five weeks old in littermate controls of *Fgfr2*$^{S252W/+}$ mice (m, o, q), *Fgfr2*$^{S252W/+}$ mice (n, p, r), littermate controls of *Fgfr2c*$^{C342Y/+}$ mice (s, u, w) and *Fgfr2c*$^{C342Y/+}$ mice (t, v, x). White arrows and white arrowheads indicate the ISS and the SOS, respectively. High magnification of the ISS (o, p, u, v) and the SOS (q, r, w, x) indicated by hatched line boxes in (m), (n), (s) and (t) are shown. Black arrowheads in (m) and (s) indicate ossification of the ISS. bo, basioccipital bone; bs, basisphenoid bone; pl, palatine bone; ps, presphenoid bone; hz, hypertrophic zone; nc, nasal cavity; pz, proliferating zone; rz, resting zone. Scale bars: 1 mm (e), 200 μm (m), 20 μm (o), 50 μm (q).

Figure 2. Hematoxylin-Eosin staining of the cranial base in *Fgfr2*$^{S252W/+}$ mice and *Fgfr2c*$^{C342Y/+}$ mice at P7 and P14.

(a, b, g, h, m, n, s, t) Hematoxylin-Eosin staining of sagittal section of the cranial base at P7 and P14 in littermate controls of *Fgfr2*$^{S252W/+}$ mice (a, g), *Fgfr2*$^{S252W/+}$ mice (b, h), littermate controls of *Fgfr2c*$^{C342Y/+}$ mice (m, s), *Fgfr2*$^{S252W/+}$ mice (s, t). High magnification of the ISS (c, d, i, j, o, p, u, v) and SOS (e, f, k, l, q, r, w, x) indicated by hatched line boxes in (a), (b), (g), (h), (m), (n), (s) and (t) are shown. bo, basioccipital bone; bs, basisphenoid bone; pl, palatine bone; ps, presphenoid bone; hz, hypertrophic zone; nc, nasal cavity. Scale bars: 200 μm (a), 50 μm (c).

Figure 3. Scatter plot of CVA analysis applied to the skulls of *Fgfr2*$^{S252W/+}$ mice and their littermate controls after the weaning period.

Closed circles, opened square, closed triangle, and opened star indicate mice at three, five, seven and nine weeks old in *Fgfr2*$^{S252W/+}$ mice (magenta) and littermate controls (black), respectively. Red arrows indicate ontogenic trajectories of *Fgfr2*$^{S252W/+}$ mice and littermate controls. The wireframes with blue lines along the CV1 axis show morphological features of the lateral view (top) and the frontal view (bottom) of the positive extreme (right, CV1= 15) and those of the negative extreme (left, CV1= –9). The wireframes with blue lines

along the CV2 axis show morphological features of the lateral view (right) and the frontal view (left) of the positive extreme (top, CV2= 10) and those of the negative extreme (bottom, CV2= –5). The gray dashed lines and landmarks indicate mean shape of all observed samples.

Figure 4. Scatter plot of CVA analysis applied to the skulls of *Fgfr2c*$^{C342Y/+}$ mice and their littermate controls after the weaning period.
Closed circles, opened square, closed triangle and opened star indicate three, four, five and six weeks old in *Fgfr2c*$^{C342Y/+}$ (pale green) and littermate controls (black), respectively. Red arrows indicate ontogenic trajectories of *Fgfr2c*$^{C342Y/+}$ and littermate controls. The wireframes with blue lines along the CV1 axis show morphological features of the lateral view (top) and the frontal view (bottom) of the positive extreme (right, CV= 15) and those of the negative extreme (left, CV= –9). The wireframes with blue lines along the CV2 axis show morphological features of the lateral view (right) and the frontal view (left) of the positive extreme (top, CV= 5) and those of the negative extreme (bottom, CV= –10). The gray dashed lines and landmarks indicate mean shape of all observed samples.

Figure 5. Scatter plot of CVA analysis applied to the skulls of *Twist1*$^{+/-}$ mice and littermate controls after the weaning period. Closed circles, opened square, closed triangle, and opened star indicate mice at three, five, seven and nine weeks old in *Twist1*$^{+/-}$ (blue) and wild-type (black) mice, respectively. Red arrows indicate ontogenic trajectories of *Twist1*$^{+/-}$ mice and littermate controls. The wireframes with blue lines along the CV1 axis show morphological features of the lateral view (top) and the frontal view (bottom) of the positive extreme (right, CV= 20) and those of the negative extreme (left, CV= –30). The wireframes with blue lines along the CV2 axis show morphological features of the lateral view (right) and the frontal view (left) of the positive extreme (top, CV= 20) and those of the negative extreme (bottom, CV= –10). The gray dashed lines and landmarks indicate mean shape of all observed samples.

Figure 6. Scatter plot of PCA analysis applied to the skulls of three CS models with synostosis of the coronal suture and their littermate controls. Closed circles with blue, magenta and pale green represent *Twist1*$^{+/-}$, *Fgfr2*$^{S252W/+}$, and *Fgfr2c*$^{C342Y/+}$ mice, respectively. Opened circles represent littermate controls of each mouse model.

Supplementary material

Figure.S1

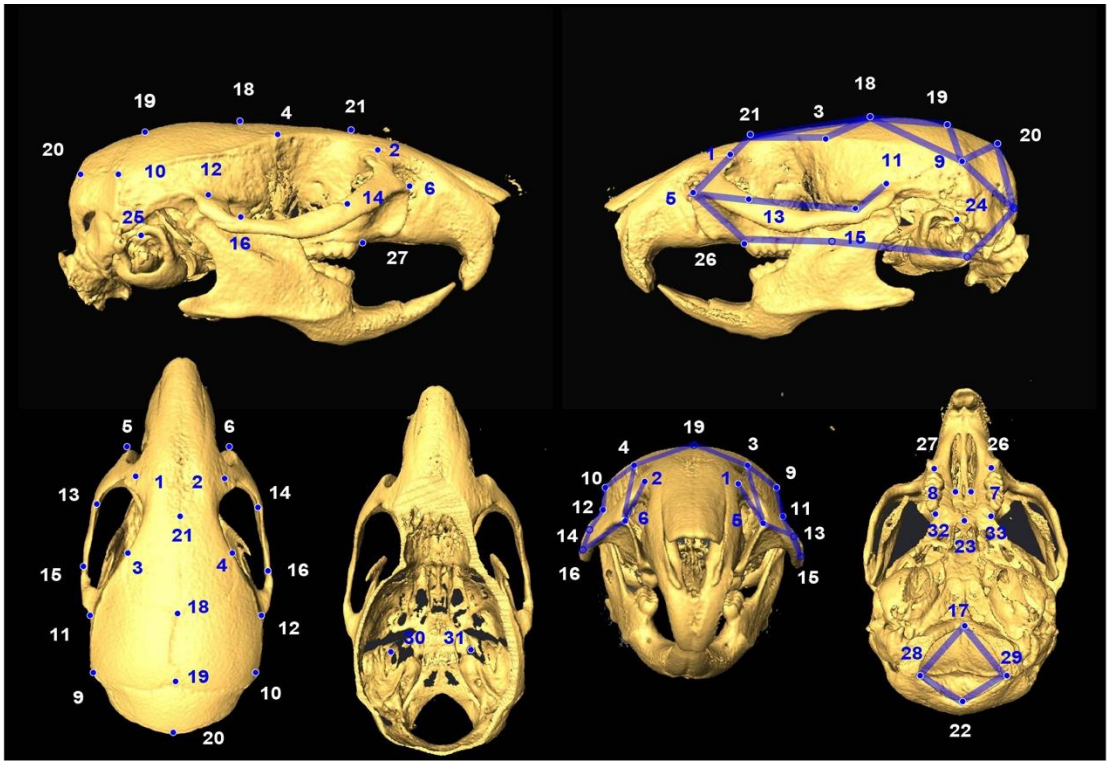

Figure.S2

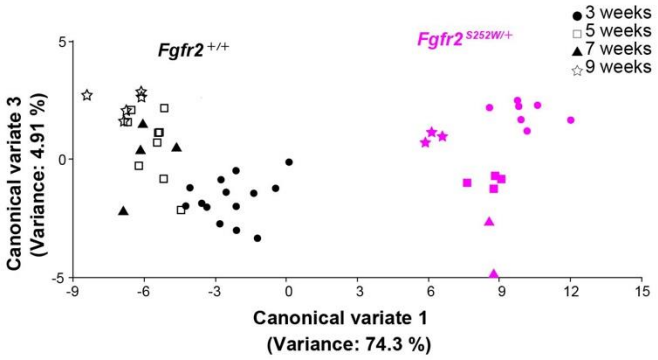
Fgfr2 +/+
Fgfr2 S252W/+
3 weeks
5 weeks
7 weeks
9 weeks
Canonical variate 3
(Variance: 4.91 %)
Canonical variate 1
(Variance: 74.3 %)
5
0
-5
-9
-6
-3
0
3
6
9
12
15

Figure.S3

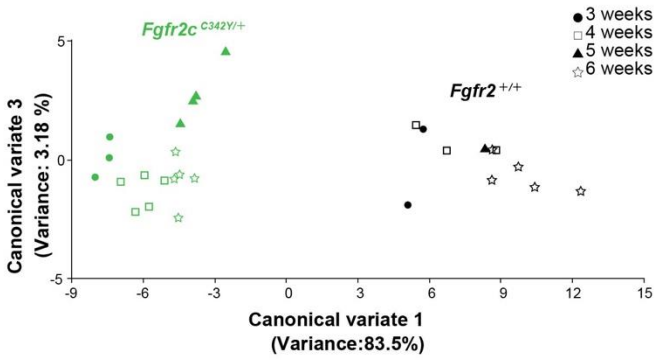
Fgfr2c C342Y/+
Fgfr2 +/+
3 weeks
4 weeks
5 weeks
6 weeks
Canonical variate 3
(Variance: 3.18 %)
Canonical variate 1
(Variance:83.5%)
5
0
-5
-9
-6
-3
0
3
6
9
12
15

Figure.S4

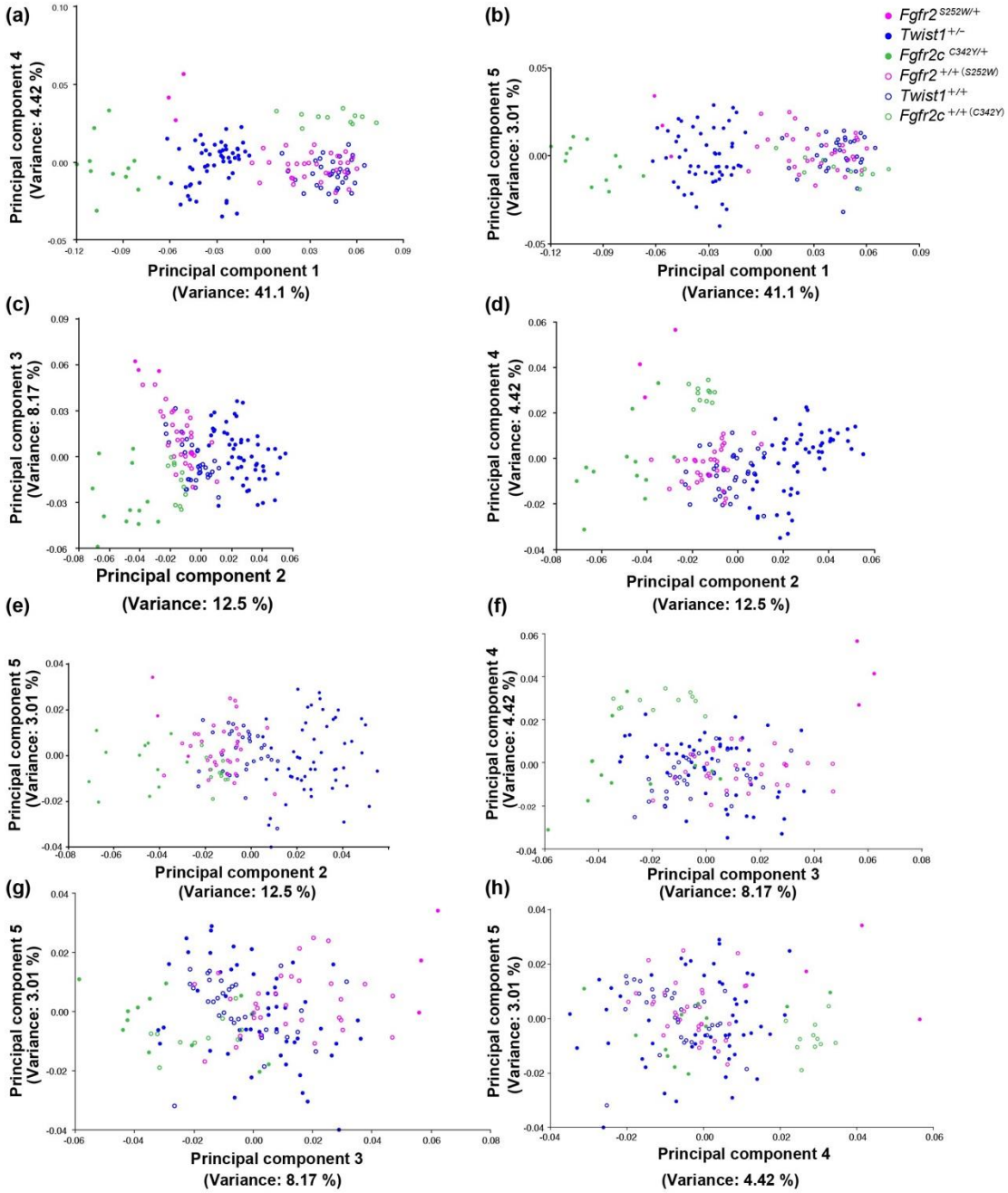
(a)
Principal component 4 (Variance: 4.42 %)
Principal component 1 (Variance: 41.1 %)
(b)
Principal component 5 (Variance: 3.01 %)
Principal component 1 (Variance: 41.1 %)
Fgfr2 S252W/+
Twist1 +/−
Fgfr2c C342Y/+
Fgfr2 +/+ (S252W)
Twist1 +/+
Fgfr2c +/+ (C342Y)
(c)
Principal component 3 (Variance: 8.17 %)
Principal component 2 (Variance: 12.5 %)
(d)
Principal component 4 (Variance: 4.42 %)
Principal component 2 (Variance: 12.5 %)
(e)
Principal component 5 (Variance: 3.01 %)
Principal component 2 (Variance: 12.5 %)
(f)
Principal component 4 (Variance: 4.42 %)
Principal component 3 (Variance: 8.17 %)
(g)
Principal component 5 (Variance: 3.01 %)
Principal component 3 (Variance: 8.17 %)
(h)
Principal component 5 (Variance: 3.01 %)
Principal component 4 (Variance: 4.42 %)

Table S1 Sample size of CVA analysis for each three craniosynostosis mouse model

	3 weeks	**5 weeks**	**7 weeks**	**9 weeks**	**Total**
Fgfr2 $^{+/+}$	14	9	4	5	32
Fgfr2$^{S252W/+}$	7	4	2	3	16
	3 weeks	**4 weeks**	**5 weeks**	**6 weeks**	**Total**
Fgfr2 $^{+/+}$	2	3	1	5	11
Fgfr2c $^{C342Y/+}$	3	5	4	5	17
	3 weeks	**5 weeks**	**7 weeks**	**9 weeks**	**Total**
Twist1 $^{+/+}$	5	10	9	9	33
Twist1 $^{+/-}$	8	15	14	15	52

Table S2 Anatomical definition of landmarks used in the analysis of the skull

Landmark No.	Abbreviations	Position of Landmarks
1	lflac	Intersection of frontal process of maxilla with frontal and lacrimal bones, left side
2	rflac	Intersection of frontal process of maxilla with frontal and lacrimal bones, right side
3	lfsq	Frontal-squasmosal intersection at temporal crest, left side
4	rfsq	Frontal-squasmosal intersection at temporal crest, right side
5	lorb	Anterior notch on frontal process lateral to infraorbital fissure, left side
6	rorb	Anterior notch on frontal process lateral to infraorbital fissure, right side
7	lpalf	Most posterior point of the anterior palatine foramen, left side
8	rpalf	Most posterior point of the anterior palatine foramen, right side
9	lpto	Intersection of parietal, temporal and interparietal bones, left side
10	rpto	Intersection of parietal, temporal and interparietal bones,right side
11	lsqzy	Joining of squasmosal body to zygomatic process of squasmosal, left side
12	rsqzy	Joining of squasmosal body to zygomatic process of squasmosal, right side
13	lzya	Intersection of zygomatic process of maxilla with zygoma , superior surface, left side
14	rzya	Intersection of zygomatic process of maxilla with zygoma, superior surface, right side
15	lzyt	Intersection of zygoma with zygomatic process of temporal, superior aspect, left side
16	rzyt	Intersection of zygoma with zygomatic process of temporal, superior aspect, right side
17	bas	Basion : midsagittal point on the anterior margin of the foramen magnum
18	brg	Bregma: intersection of frontal bones and parietal bones at midline
19	pari	Intersection of parietal bones with anterior aspect of interparietal bone at midline
20	paro	Intersection of interparietal bones with squamous portion of occipital bone at midline
21	nas	Nasion: Intersection of nasal bones, caudal point
22	opi	Opisthion : midsagittal point on the posterior margin of the foramen magnum
23	pns	Posterior nasal spine, most posterior projection of the posterior nasal spine
24	leam	Most poteroinferior point on the superior portion of the tympanic ring, left side
25	ream	Most posteroinferior point on the superior portion of the tympanic ring, right side
26	lama	The anterior most point on the central ant/post axis of the left molar alveolus
27	rama	The anterior most point on the central ant/post axis of the right molar alveolus
28	rfmc	Intersection of the right occipital condyle and the foramen magnum, taken at the lateral most curvature, right side
29	lfmc	Intersection of the right occipital condyle and the foramen magnum, taken at the lateral most curvature, left side
30	riam	Internal acoustic meatus, right side, most inferomedial point
31	liam	Internal acoustic meatus, left side, most inferomedial point
32	rpma	The posterior most point on the central ant/post axis of the right molar alveolus
33	lpma	The posterior most point on the central ant/post axis of the left molar alveolus

Figure S1. Location of landmarks collected from 3D reconstructions of μCT images of mouse skulls. Landmarks in right and left lateral (top), and superior, endocranial, frontal, and inferior views (bottom) on the μCT data of the skull in the wild-type mouse. Wireframes for indicating morphological variation related to CVA are displayed with blue lines. Definitions of each landmark are described in Table S2.

Figure S2. Scatter plot of CVA applied to the skulls of *Fgfr2*$^{S252W/+}$ and their littermate controls. Closed circles, opened square, closed triangle, and opened star indicate mice at three, five, seven and nine weeks old in *Fgfr2*$^{S252W/+}$ mice (magenta) and littermate controls (black), respectively. The distribution of each mouse along CV1 and CV3 is shown.

Figure S3. Scatter plot of CVA applied to the skulls of *Fgfr2c*$^{C342Y/+}$ and their littermate controls. Closed circles, opened square, closed triangle, and opened star indicate mice at three, four, five and six weeks old in *Fgfr2c*$^{C342Y/+}$ mice (pale green) and littermate controls (black), respectively. The distribution of each mouse along CV1 and CV3 is shown.

Figure S4. Scatter plot of PCA applied to the skulls of three CS models having synostosis of coronal suture and their littermate controls. Closed circles with blue, magenta, and pale green represent *Twist1*$^{+/-}$ mice, *Fgfr2*$^{S252W/+}$ mice, and *Fgfr2c*$^{C342Y/+}$ mice, respectively. Opened circles represent littermate controls of each mouse model. The distributions of each mouse along PC1–PC4 (a), PC1–PC5 (b), PC2–PC3 (c), PC2–PC4 (d), PC2–PC5 (e), PC3–PC4 (f), PC3–PC5 (g) and PC4–PC5 (h) are shown.